New preparation method of microstructurally and mechanically standardized PETG specimens by material extrusion additive manufacturing and machining

Geoffrey Ginoux, Joseph Paux, Samir Allaoui

New preparation method of microstructurally and mechanically standardized PETG specimens by material extrusion additive manufacturing and machining

GEOFFREY GINOUX, JOSEPH PAUX, SAMIR ALLAOUI

Institut de Thermique, Mécanique, Matériaux (EA 7548), MATUR Chair, University of Reims Champagne-Ardenne, EiSINe, Campus Sup Ardenne,

08000 Charleville-Mézières (France) – Email: geoffrey.ginoux@univ-reims.fr

Abstract.

Additive manufacturing processes are recent and lack standardized methods to characterize the mechanical properties of the printed material. Sample preparations in the literature consist in the direct printing of specimens, which induces uncontrolled interactions between printing conditions of the specimens and material properties. This study aims to develop a method for the specimen preparation to characterize the behavior of materials manufactured by material extrusion additive manufacturing. The proposed method consists in preparing printed plates from polyethylene terephthalate glycol-modified filament into a unique design before machining out specimens at different orientation angles. A comparison to directly printed specimens at the same orientation angles is performed to confront the proposed method to a commonly used one in the literature, and to understand the cause of discrepancies and the lack of predictiveness in additive manufacturing. The prepared specimens are characterized by X-ray tomography and tensile tests to assess process-structure-property relationships. The analysis highlights the structure heterogeneity of the as-printed specimen compared to the machined one, which influences the mechanical properties of the specimen. The new hybrid additive-subtractive preparation method for the specimen limits the superimposed thermo-kinetic effects caused by changes in deposition strategy, including coalescence and flow instability, and allows to measure effective mechanical properties based on a homogenized multiscale structure that is more representative of large parts. In addition, machining smooths the surface without thermal alterations, which leads to more accurate mechanical testing regarding cross-sectional area measurement, crack initiation and fracture mode. The proposed method is thought to standardize the preparation of additively manufactured materials based on extrusion to ease comparison between studies, to help the qualification of technical and industrial parts, and to measure intrinsic material's properties based on a controlled microstructure for understanding of the process-related behavior and properties of material.

Keywords: Fused filament fabrication, methodology, tomography, tensile test, process-property relationship.

1. Introduction

Additive manufacturing (AM) based on material extrusion, also known as Fused Filament Fabrication (FFF), has developed since the 1980s and has most recently gained interest for its ease-of-use and cost-effectiveness [1]. Due to the layer-by-layer AM, the technology appears useful to produce parts with complex geometries. However, this manufacturing technique tends to manufacture porous and anisotropic parts with inferior mechanical properties compared to conventionally manufactured parts by formative or subtractive processes [2,3]. The relatively poor mechanical properties hinder the use of this technology for the manufacturing of technical and/or small-series end-products [4], which require development of improvement methods and materials to enable the technology to reach applications with high demands such as aerospace or biomedical [5,6].

Literature reports several studies on parametric optimization to improve and reduce this gap of mechanical performance [7–9]. Among the different printing parameters, geometric parameters affecting the deposition strategy – namely layer height, raster orientation, filling rate, etc. – are the most impacting on the mechanical properties [10]. Beside the direct effects of geometric parameters on the structure and the induced properties, thermo-kinetic phenomena are noticed and indirectly play a major role on the mechanical properties and therefore should be addressed [11]. These phenomena include internal residual stress and warping [12], coalescence and inter-raster/inter-layer sintering [13], or vibration and ringing [14]. Although those phenomena are directly affected by the thermo-kinetic parameters, such as nozzle temperature or printing speed [7], the geometric parameters can indirectly affect those same phenomena. The effects are explained by the heating/cooling cycling during changes in trajectory length [15], or the nozzle/material or raster/raster heat exchange rates via changes in flow rate or area of raster section with layer height [16,17], or even the number, length and trajectories of rasters and therefore the acceleration/deceleration occurrences [18]. Those phenomena affect the local behavior of the parts, which mingle the intrinsic behavior of the materials with the effects induced by the process. Therefore, studies need to prepare standardized specimens to characterize the intrinsic properties before including process-induced effects regarding chosen configurations to separate the superimposed effects. However, the effects of the process and deposition strategy can vary from one preparation method to another with different sample geometries or dimensions due to a scale effect. A comparison between the specimen geometries according to different standards already showed disparities in mechanical performance due to a change in raster-to-contour ratio [19], which proves the need to standardize the preparation methods as dimensions of tensile test specimens are expected to modify the process-induced microstructure and then the mechanical properties. It appears a lack of standardization to control those phenomena and allows the comparison between the numerous studies [20], but also to properly estimate the effective properties.

Several studies developed preparation methods of additively manufactured specimens with the aim of standardizing or estimating effective properties. Fang *et al.* [21] recently estimated the effective Young's moduli of FFF-manufactured materials by printing a box consisting of single-raster walls and then cutting specimens at different orientations from the walls. The hybrid additive-subtractive preparation method, coupled with numerical simulations, succeeded with a good accuracy to estimate the mechanical properties, but the method is limited to the study of thin-wall samples which may not be representative of technical and full parts. Other studies tried the printing of plates before cutting by water jet to standardize the printing of a unique part before preparing the tensile test specimens out of the plates [19,22]. Water jet was used to avoid thermal alterations of the mesostructure around the edges, compared to conventional machining methods such as drilling where frictions are not negligible, but still led to an increased variability on the mechanical properties. On the opposite, Song *et al.* [23] performed a conventional machining on printed blocks to eliminate edge effect and did not notice thermal alterations on the mesostructure, but different blocks at various parameter settings were used rather than a unique standardized part. Thus, this method may still include process-induced phenomena based on the geometry and deposition strategy. It appears from the literature a need for complementary studies to fill the gap linking the process to the material properties.

One way to control the process-induced properties is the characterization of the microstructure. Conventional methods include microscopy of cross-sectional areas or X-ray micro-computed tomography (X-μCT) of the part. Most of the studies use microscopy as the method is less expensive and easier to handle. However, the method is limited to static and ex-situ observations and must assume a constant structure along the deposition path that may not be true if considering variability and defects, and their effects on the mechanical response [24].

It appears from the literature a lack of fundamental understanding of the material properties in AM as printed specimen properties depend on parametric factors, specimen geometry and, subsequently, process-induced microstructure. As intrinsic properties are not characterized away from structure properties in a systemic manner, studies in the literature might be subject to discrepancies between them and would explain the limited predictiveness of printed specimen properties. The aim of this study is to propose a standardized design and method to free the sample preparation and effective mechanical properties from structure properties, namely edge and scale effects, with the idea to develop a standardization method for fundamental understanding of material-structure-process in AM, study comparison, industrial qualification, and measurement of effective properties of engineering parts. The developed method consists in printing plates from a unique design then in machining tensile test specimens at different orientation angles to obtain a standardized microstructure between the different deposition strategy. The proposed method is compared to a direct FFF method to assess the process-properties relationships and the differences in phenomena between the two methods. All samples are analyzed by X-μCT and tensile tests to link the process to the induced microstructure, and then to the mechanical properties. The microstructure is characterized concerning both global structure and structure variability to compare and separate the effects on the macrostructure from those on the microstructure.

2. Materials and methods

2.1. Specimen preparation methods

This study compares two preparation methods of samples for structural and mechanical analyses. The first method involves the direct printing of tensile test specimens, while the second one consisted of printing plates before machining the tensile test specimens from them. Six sets of samples were manufactured for both methods with orientation angles at 0°, 15°, 30°, 45°, 60° and 90° to assess the effect of raster orientation on microstructure and mechanical properties regarding preparation method and deposition strategy.

Printed specimens were manufactured from polyethylene terephthalate glycol-modified (PETG) filament thanks to a Composer A4 printer from Anisoprint (Russia) using a material extrusion additive manufacturing (MEAM) technology. PETG filament under PolyMaxTM brand from Polymaker (France) was supplied by Imprimante3DFrance (France). Technical data is detailed in Table 1. Filament was dried in an eSun Lite filament drying box of 35 W heating power from eSun (China) at 70 °C for 8 h before use and was continuously dried in the same drying box at 70 °C during use to prevent any moisture during the AM step.

Table 1. Physical properties of PolyMax™ PETG as supplied by Polymaker.

Properties	**Values**
Diameter	1.75 ± 0.04 mm
Density (21.5 °C)	1.25 g/cm^3
Glass transition temperature	79 °C
Melt index (240 °C, 2.16 kg)	17.1 g/10 min
Young's modulus	1523 ± 50 MPa
Tensile strength	31.7 ± 0.1 MPa
Elongation at break	4.4 ± 0.6 %

The movement axes were thoroughly lubricated with supplier lubricant before printing campaign to minimize vibrations that could affect the flow stability and then the structure [14]. All specimens are measured in thickness to ensure there was no over-compression nor under-compression of the structure due to a misleveling of the build plate that could have modified the microstructure from one sample to another [22].

For the as-printed (AP) specimens preparation method, several sets of five tensile test specimens were directly printed at orientation angles of 0°, 15°, 30°, 45°, 60° and 90° and according to the type 1B design and dimensions from the ISO 527-2 standard (see Figure 1). Fixed printing parameter settings are detailed in Table 2 and were set in Aura software version 0.9.21.3 from Anisoprint. Infill orientation was constant and aligned with the X-axis of the build plate between all tensile test specimens (see Figure 2). Each set of samples was printed at a different tensile test specimen orientation angle α, meaning that the specimens were oriented with regard to the build plate axes to keep the same raster orientation compared to the build plate axes, i.e. the same displacement direction of the nozzle, to avoid any machine-induced variation in the deposition flow.

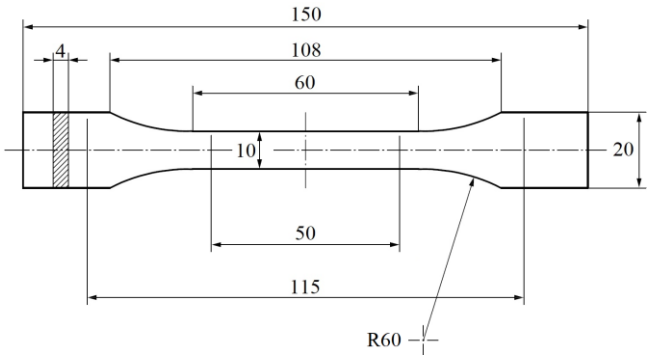

Figure 1. Type 1B tensile test specimen according to ISO 527-2 standard. Dimensions are expressed in millimeter.

Table 2. Printing parameters and associated values for the AM of tensile test specimens and plates.

Parameters	**Values**
Printing speed	50 mm/s
Nozzle temperature	235 °C
Build plate temperature	60 °C
Nozzle diameter	0.4 mm
Raster width	0.4 mm
Layer height	0.2 mm
Infill orientation (X-axis)	0°
Fill density	100%
Number of perimeter contours	1

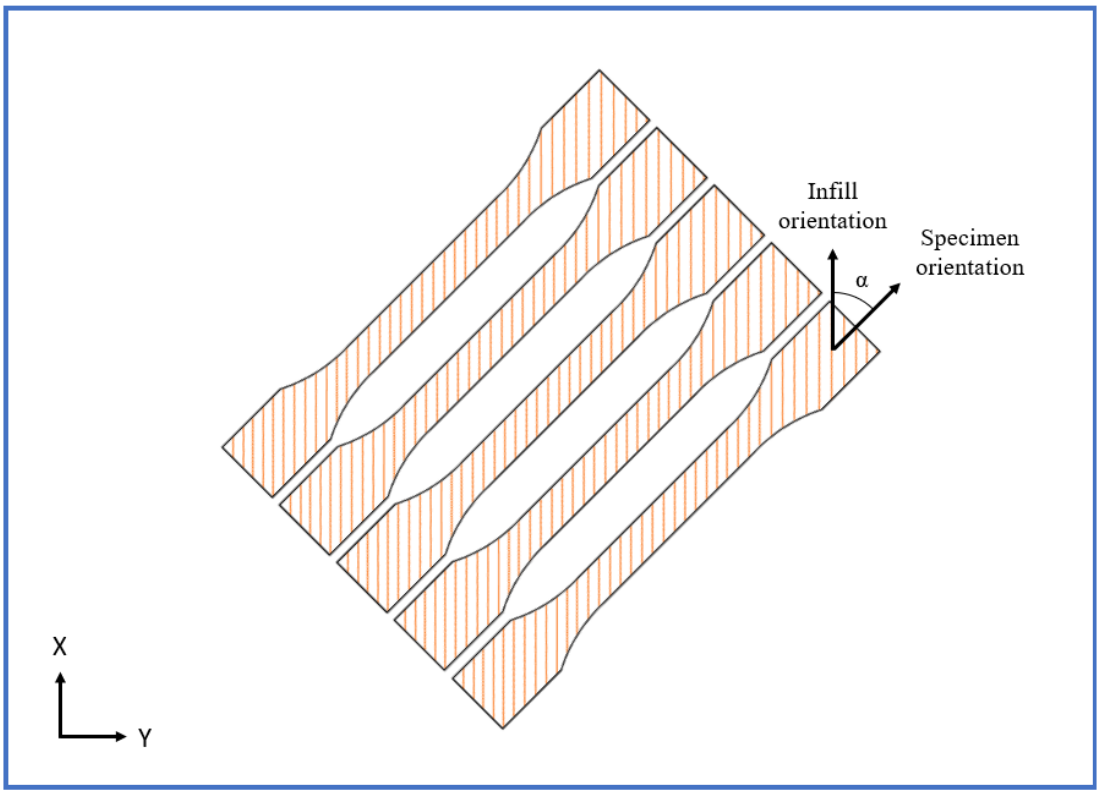

Figure 2. Schematic 2D representation of a set of five tensile test specimens (in black contour) on the Composer A4 build plate (in blue contour) with an example of orientation angle α of 45° between specimen orientation and infill orientation (in orange), in comparison to the X-Y axes of the build plate.

The machined specimens from printed materials were prepared by drilling into printed plates and are denoted as machined into printed plate (MPP) specimens. The plate design (see Figure 3) consists of (i) a rectangular shape to standardize the thermal history by printing rasters of the same length to avoid difference in heating-cooling cycles and then in inter-raster coalescence [25] in the zone where gauge sections of tensile test specimens are machined, and (ii) a circular shape where uniformity is not sought and is preferred as minimal in surface as possible for cost savings while allowing the inclusion of the grip zones of tensile test specimens for all the specimen orientations. PETG plates were printed with the same Composer A4 printer and printing parameters (see Table 2) as for AP tensile test specimens to keep as minimal as possible the differences in AM process. The AM of the plate was identical for the preparation of all MPP specimens, regardless of the specimen orientation, to obtain the same process and induced microstructure for all the plates. The plates were oriented to align the infill orientation with the length of the rectangular shape to obtain a regular deposition (see Figure 4). The plates were then drilled with a CRI1500 machining machine from Charlyrobot (France) equipped with a 2 mm drill rotating at 20000 rpm with a feed of 3000 mm/min. The machining was controlled with Fusion 360 software version 2.0.14337 from Autodesk (USA). Six sets of five type 1B tensile test specimens (see Figure 1) were machined into the printed plates with a specimen orientation of 0°, 15°, 30°, 45°, 60° and 90° compared to the orientation of the rasters (see Figure 4). The gap between the edges of the plate and the specimens is at least 11 mm. Plate design in STL format for AM and tensile test specimen design in STL and STEP formats for, respectively, AM and machining are supplied in Supplementary material. One should note that the current study is focused on the in-plane properties corresponding to the XY plane. For translatability to the XZ and the YZ planes, a double vertical plate positioned with a relative 90° angle to prevent printing from failing because of imbalance could be printed. Print strategy and part design and dimensions may differ in thermal

history, and then in microstructure and mechanical properties [25], which would require other considerations and additional experimentation to confirm the translatability to planes other than the studied XY plane.

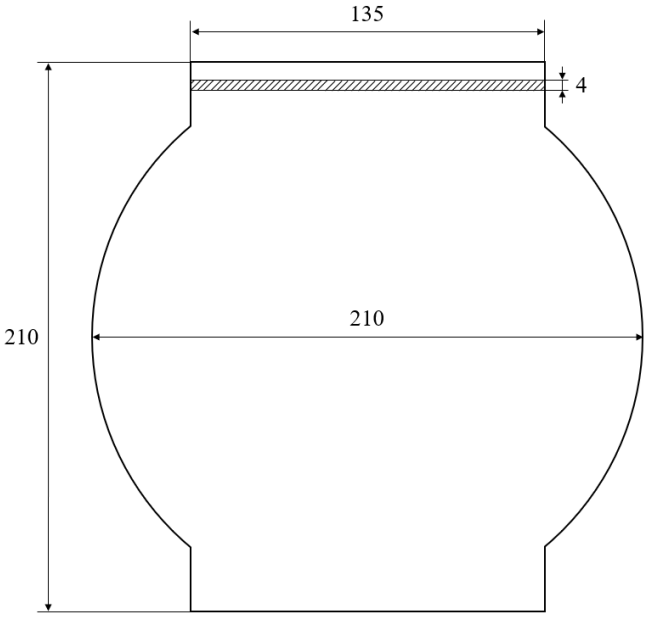

Figure 3. Printed plate design for machining of a set of five type 1B tensile test specimens that can contain all specimen orientations. Dimensions are expressed in millimeter.

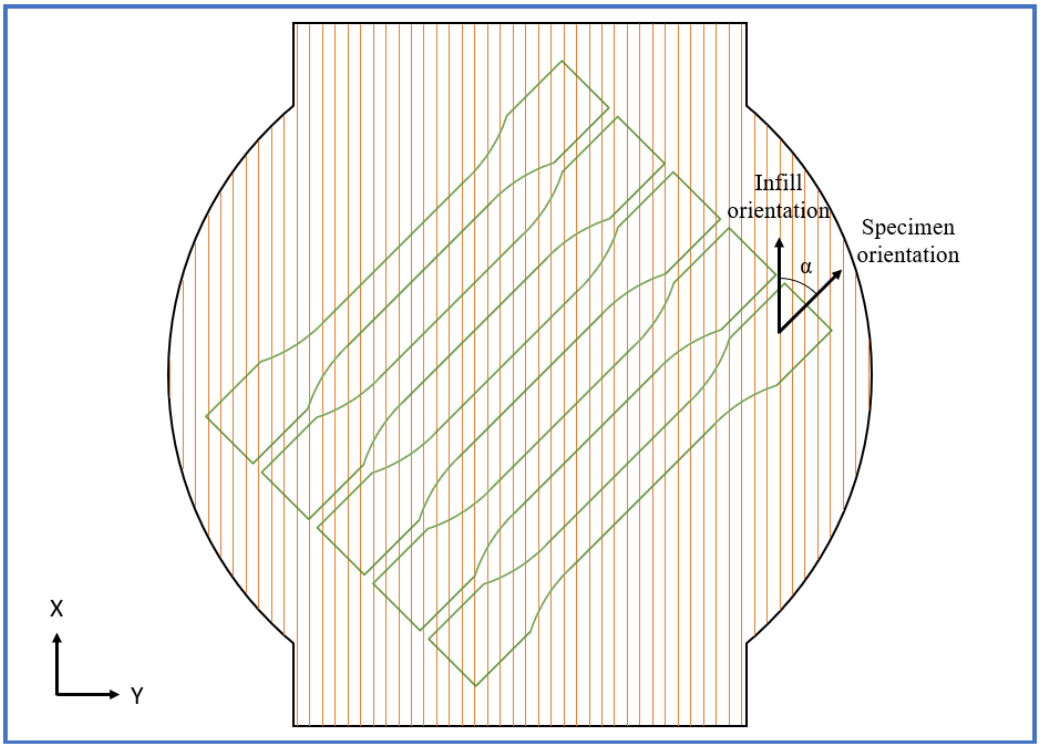

Figure 4. Schematic 2D representation of a printed plate (in black contour) on the Composer A4 build plate (in blue contour) oriented in the length of the rectangular shape with the X axis of the build plate, with an example of drill path (in green contour) after printing for the machining of a set of five tensile test specimens oriented at a specimen orientation angle α of 45° compared to the infill orientation (in orange).

2.2. Characterization tests

Microstructures in the gauge section of tensile test specimens were analyzed by X-µCT with a Desk-Tom 150 from RX Solutions (France). The scanning step used an X-ray source with a voltage of 60 kV and a current intensity of 166 µA with a 1920 x 1536 pixels scintillation detector. The scanning consisted of 1440 radiographic images at 1.7 images/s with a voxel size of 5.0 µm. Once 2D images acquired, the 3D volume reconstruction is carried out on X-Act software version 2.0 from RX Solutions. For qualitative observations of the microstructure, a right rectangular prism of 5.0 x 10.5 x 4.5 mm^3 was selected around the middle of the gauge section of tensile test specimens and oriented with the specimen orientation to observe the whole width and thickness of the gauge section (see Figure 5(a)). For quantitative measurements of the microstructure, a right rectangular prism of 4.4 x 4.4 x 1 mm^3 was selected in the middle of the gauge section, to avoid local irregularities like small pores in the first layers [26]. A 4.4 x 4.4 x 1 mm^3 right rectangular prism was also oriented with the raster orientation to observe the evolution of porosity in the core zone along the deposition path with the same observed rasters from the first to the last sectional cut orthogonal to the X direction (see Figure 5(b)). Raw data of pre-treated volumes were then numerically treated to calculate the sectional porosity of the successive cuts orthogonal to the X direction.

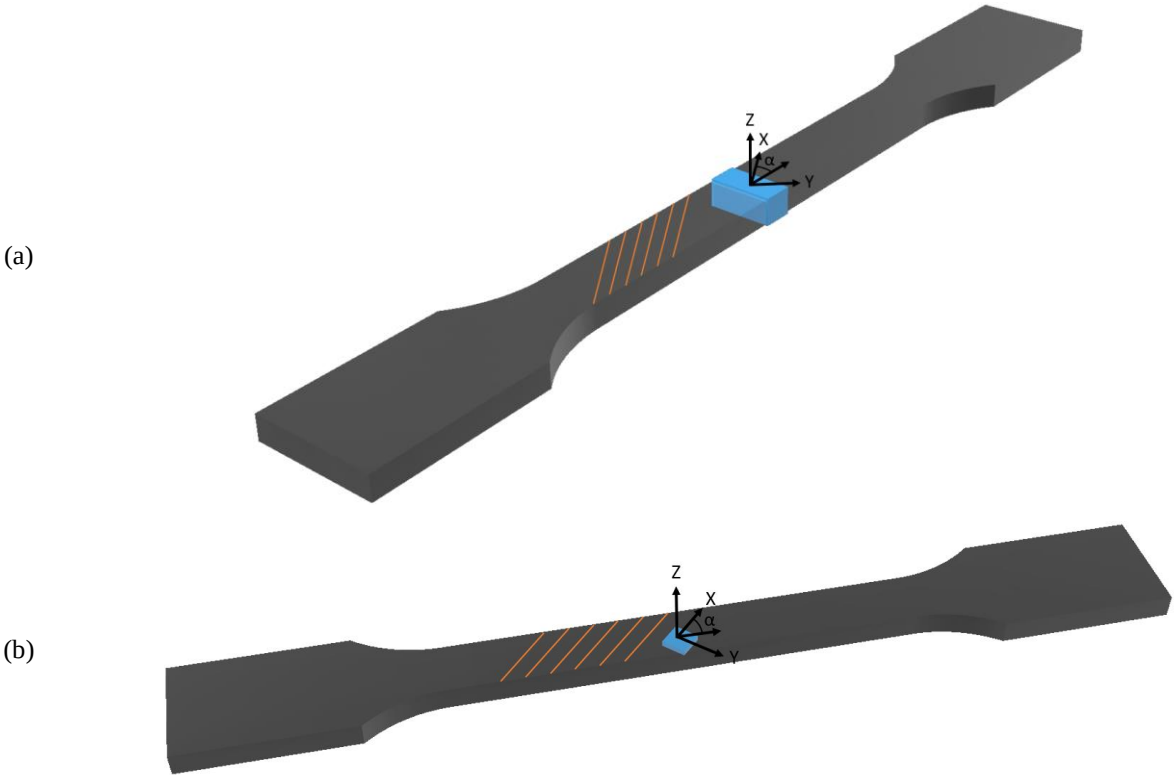

Figure 5. Schematic 3D representations of numerically treated volumes (in blue) from X-µCT data for (a) qualitative observations and (b) quantitative measurements of the microstructure of type 1B tensile test specimens (in transparent grey) with the example of specimens oriented to an orientation angle $\alpha = 45°$ compared to the infill orientation aligned in the X direction (partial representation of printed rasters in orange).

The mechanical properties were measured on a universal testing machine Instron 3366 (USA) with a 10 kN load cell and a video extensometer. Tensile tests were performed at a 1 mm/min crosshead speed at room temperature of 21 °C. The video extensometer was used to record the sample strains during tensile test with the help of two white marks of 2 mm in

diameter separated by a 50 mm distance and centered in the middle of the gauge section surface. All samples were measured in thickness and width three times with an ABS Digimatic electronic caliper from Mitutoyo (Japan) with a 0.01 mm precision to calculate the specimen's section. All sample configurations were measured five times. Dixon tests were carried out to check the absence of anomalous values.

3. Results and discussion

3.1. Microstructure

The different internal layer microstructures of AP and MPP tensile test specimens in the whole width of the gauge section are illustrated in Figure 6. The AP specimens show three microstructural zones:

- The first one is the single-raster contour that has a constant width for all the AP specimens and is designated as the perimeter.
- The second zone is the U-turn due to the back-and-forth trajectory of the raster deposition. This microstructure is absent in the 0° specimen as U-turn is achieved in the grip and shoulder sections, i.e. outside of the gauge sections. The greater the angle is, the wider the U-turn zone is, as the back-and-forth trajectory is more and more aligned with the width direction of the tensile test specimen. The U-turn zones present a fuller microstructure inside the turns due to the deposition trajectory, leading to narrower porosities on one side alternating from edge to edge. As deceleration occurs when performing the U-turn, residence time in the nozzle increases and leads to higher temperatures [27] and then to more coalescence [13]. Like perimeter contour, this fuller microstructure contributes to more cohesive adhesions on the edges of the specimens.
- The third and last zone is the core zone where the rasters follow their straight trajectory for part filling. The core volume fraction represents around 91.3% of the total gauge section for a specimen oriented at $\alpha = 0°$ and decreases with α down to 64.5% of the total gauge section for a specimen oriented at $\alpha = 90°$. In addition, the deposited rasters appear wavier when increasing α and are explained by shorter acceleration/deceleration cycles that lead to vibrations [14] and then to disturbed flow.

On the contrary, the MPP specimens present a single microstructural zone that is equivalent to the core zone of the AP specimens with a more linear and regular profile. Consequently, the MPP specimens have a more homogeneous structure consisting of fully unidirectionally oriented rasters, whereas AP specimens present non-unidirectionally oriented structures on the edges, and, in the gauge section, a perimeter aligned with the specimen orientation. Then, the larger the orientation angle is, the wider the fraction of the non-unidirectionally oriented structure is, from one tenth to one third of the total architecture. This difference of structure can cause a non-negligible edge effect impacting the global tensile properties of the AP specimens at different amplitudes from one orientation angle to another. The experimental mechanical properties of the AP specimens are then not expected to be representative of the mechanical properties of the core zone of the specimen. Consequently, their properties cannot be extended to larger parts where the perimeter and U-turn zones can be negligible compared to the core zone, and more generally to parts printed with deposition strategy and/or geometries involving long rasters and few U-turns.

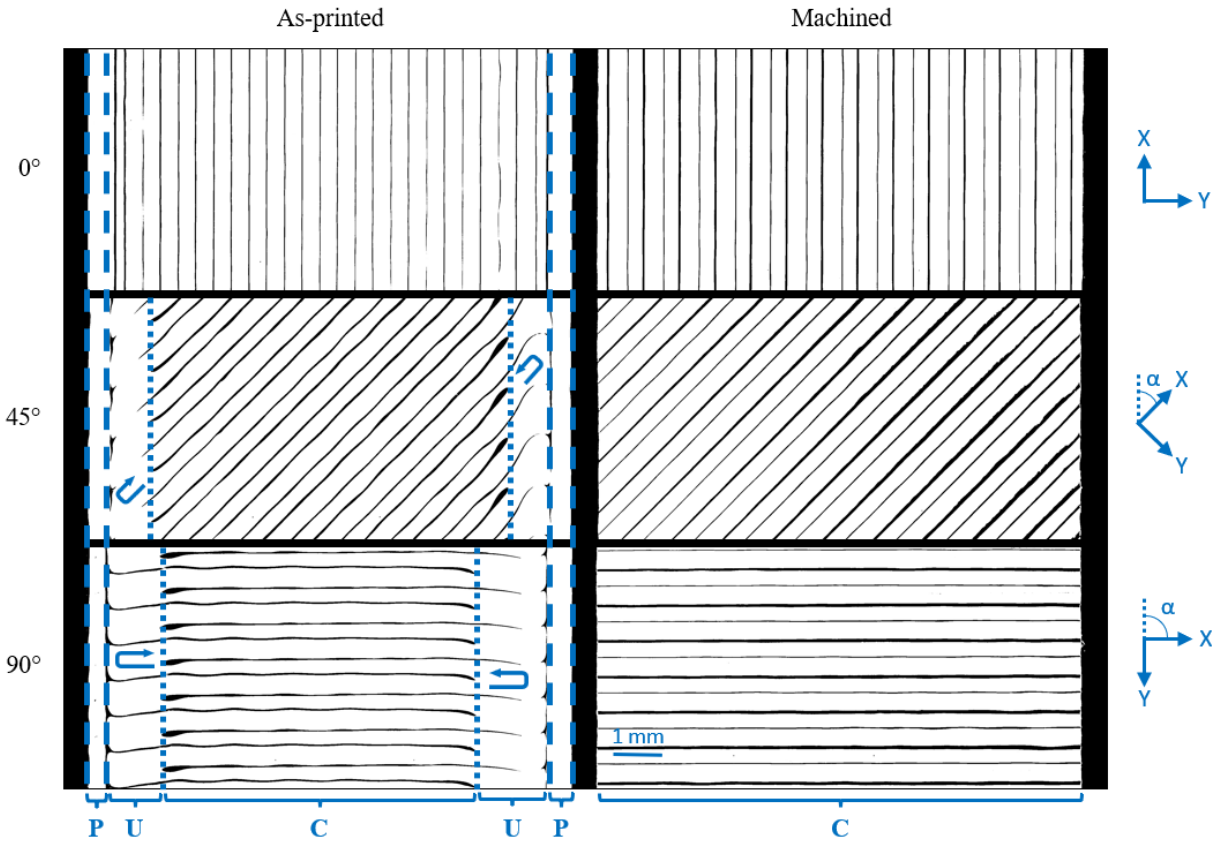

Figure 6. X-µCT cuts orthogonal to the Z direction in the gauge section of AP and MPP PETG tensile test specimens, with a specimen orientation angle α compared to the X axis of 0°, 45° and 90°. (P) zones delimit the perimeter zones, (U) zones delimit the U-turn zones, and (C) zones delimit the core zones. U-arrows represent the deposition path in the U-turn zone.

The effective sections of the tensile test specimens, on which the tensile stress is applied, are displayed in Figure 7. For all specimens, more coalescence occurred at the bottom of the specimen and lead to smaller porosities due to the heating build plate needed for part adhesion [26]. This heat excess also leads to more fluid polymer depositions and then to collapsing rasters with a porosity shift out of its initial trajectory leading to a wider specimen at the bottom up to 4%. The hybrid AM/machining preparation method removes this material excess located in the contours of the plates and therefore lead to specimens that are more dimensionally homogeneous, with a more precise section, and without asperities on the edges. The overall structure is then more constant along the Z direction with the MPP specimens compared to the AP ones. One should note that the MPP specimens show no apparent alterations of the edges and surroundings that could have happened during machining post-processing, like crack damage or delamination [28]. Little re-melting due to the frictions is still observed on the smoothed surface but does not exceed 24 µm in width (see MPP specimens in Figure 7), which is not expected to be critical on the general mechanical behavior. This observation may not be true with other polymeric materials, especially with more thermo-sensitive polymers like PLA, but is expected to be true with technical polymers like PEEK that presents higher thermomechanical resistance compared to PETG.

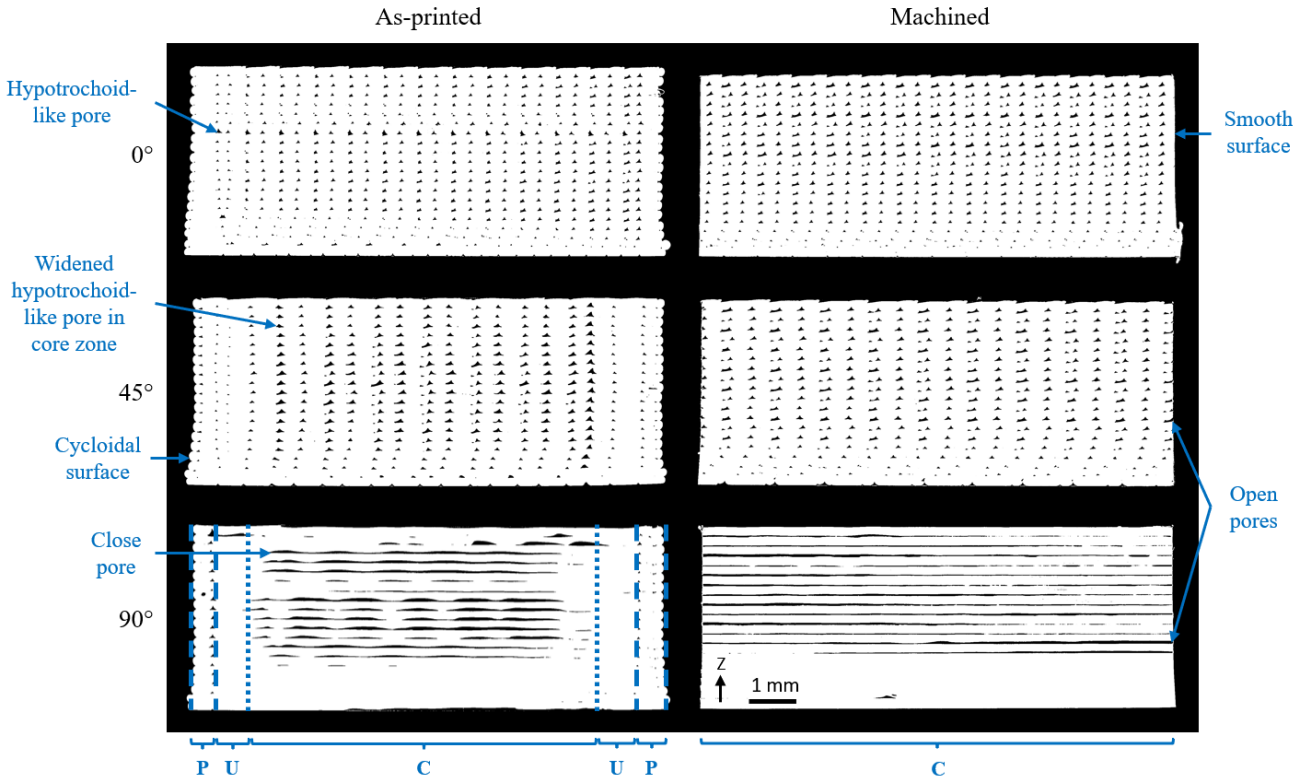

Figure 7. X-µCT cuts orthogonal to the tensile test specimen orientation in the gauge section of AP and MPP PETG specimens, with a specimen orientation angle α compared to the X axis of 0°, 45° and 90°. Blue annotations indicate examples of the different observed morphological features and their relative positioning in the perimeter zone (P), the U-turn zone (U) and the core zone (C).

As previously observed in Figure 6 with 0°-oriented AP specimens, the edge microstructure is consistent with the microstructure in the core zone for the AP specimens when filled in the same direction as the direction of the perimeter deposition (see 0° AP specimen in Figure 7). When increasing the orientation angle, the hypotrochoid-like porosities in the core zone are wider while the porosities around perimeter are still of low dimensions (see 45° AP specimen in Figure 7). Ultimately, at 90° orientation angle for the AP specimens, large porosities are observed along the width of the section in the core zone, but the gauge section still presents small porosities around the perimeter and fuller microstructure between perimeter and core zones with effective inter-layer coalescence in the U-turn zone (see 90° AP specimen in Figure 7). On the contrary, for the MPP specimens, large and homogeneous porosities extend from edge to edge, except at 0°, leading to open pores (see 45° and 90° MPP specimens in Figure 7). On the one hand, the two preparation methods lead to different surface conditions for the specimens: for the AP specimen, the surfaces are made of cycloids (see AP specimens in Figure 7), which can act as crack initiation sites, while the MPP specimens have smooth surfaces but with open pores which may also play a part in crack initiation. On the other hand, lateral zones with good coalescence for the AP configurations can lead to better mechanical strength. The microstructures are also different in the core zones between the AP and MPP specimens regarding linearity of the raster/void interfaces (see 90° AP and MPP specimens in Figure 7). On the one hand, with the AP tensile test specimens, the depositions appear wavy. On the other hand, with the MPP specimens, the depositions are straighter. For comparison between the different specimen orientation angles and the two preparation methods, the microstructures need to be detailed cut by cut along the direction of the deposition to study the variability.

Only the core zone in the gauge section where rasters are all unidirectionally oriented is treated as the zone of interest to study the unidirectional properties of the printed samples (see Figure 5(b)). The microstructure of the section consists of circular-like sections of polymer raster and hypotrochoid-like sections of the longitudinal voids as already described in the literature [2]. The porosity of each cut along the X axis is then represented in Figure 8 to highlight the variation of microstructure during the deposition of the polymer rasters. Although the general architecture of the section remains the same, the porosity oscillates along the printing direction. This phenomenon is explained by the deposition irregularity that can occur due to a variation in feed stock flow rate [29], during inconsistent flow at nozzle exit [7], or by the vibrations caused by acceleration-deceleration cycles which lead to a micro-inconstant flow rate [14]. The process-induced microstructure is then dependent of the deposition history and vary from plane to plane. Observation of one cut along the printing direction is not enough to characterize the microstructure of the material and X-µCT analysis is necessary to analyze the complexity of the microstructure, especially concerning the actual global porosity and its distribution.

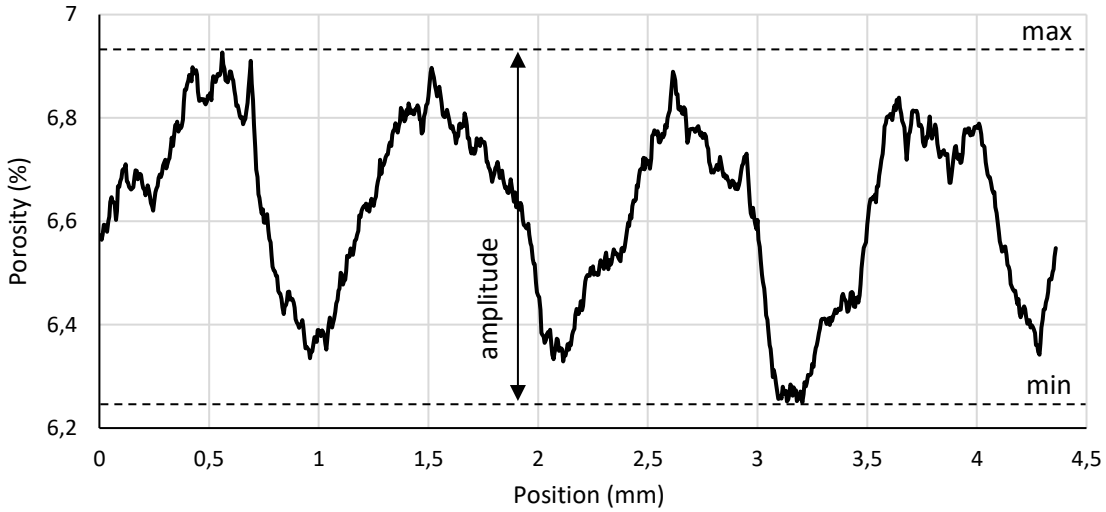

Figure 8. Porosity of the different sections along the X direction for an example of AP specimen oriented to an angle of 30° in the core zone of the gauge section as measured from treated X-µCT reconstruction.

The differences in the variations of mean porosity between the two methods of specimen preparation and regarding the orientation angle of the tensile test specimen in the core zone of the gauge section are highlighted in Figure 9. For the AP specimens (see Figure 9(a)), mean porosity tends to increase then to decrease with the orientation angle of the printed specimens. This non-monotonic influence can be explained by the influence of two effects:

- Due to more back-and-forth trajectories that cause vibrations, the greater the orientation angle is, the more unstable the flow is, which leads to defects of raster surface contacting and so to local increase of porosity [7]. Figure 6 illustrates this phenomenon with a wavier raster in the core zone from 0° to 90° for the AP specimens.
- The greater the orientation angle is, the shorter the trajectory path in a back-and-forth deposition is. The time between two adjacent raster depositions is then reduced and the raster temperature is higher, increasing the intra-layer sintering phenomena at zero-shear rate especially if temperature is above the glass temperature [17], which decreases the porosity.

Both phenomena have competitive effects on the relation between mean porosity and raster angle of the AP specimens (see Figure 9(a)). Indeed, the instability of the flow tends to increase mean porosity with raster angle while the shorter trajectory

path induces thermo-kinetic effects which decrease mean porosity with raster angle. On the contrary, the porosity oscillation amplitude along the printing direction increases monotonously with the raster angle as displayed in Figure 10. Indeed, only the flow instability, which increases with the raster angle, is involved in this phenomenon.

For the MPP specimens (see Figure 9(b)), mean porosity is constant regarding the orientation of the specimen as they come from the exact same deposition strategy of the plates in opposition to the AP specimens. As trajectory path is longer for printed plates than any of the AP tensile test specimens, the time between two adjacent rasters is high enough to let the temperature cool at the point the sintering is limited. The mean porosity of the MPP specimens is then superior to the overall porosity of the AP specimens as coalescence did not occur to decrease the pore size (see Figure 9). However, longer trajectory paths allow a more stable flow and thinner porosity distribution for printed plates. The amplitude of porosity for all the MPP specimens is then similar to that of the AP specimens with the longest trajectory paths, i.e. the 0° orientation angle (see Figure 10). Like mean porosity, the unique deposition strategy with the MPP specimens creates a single and homogeneous microstructure in the whole part regardless of the orientation angle in opposition to the AP specimens, as can be observed with a more constant raster in Figure 6 and a zero slope in Figure 10 for the MPP specimens, leading to a porosity amplitude up to six times lower than the maximum amplitude of the AP specimens (see Figure 10).

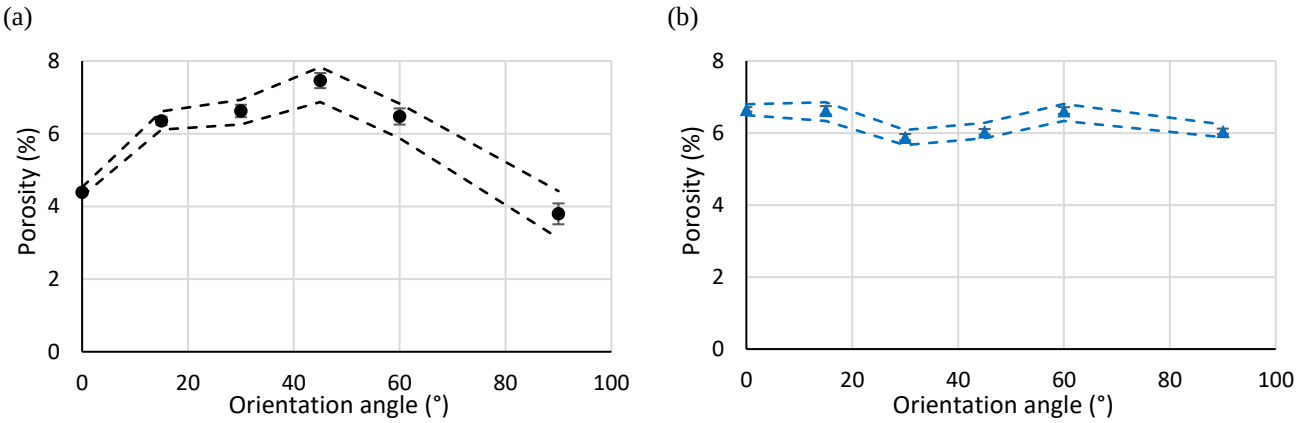

Figure 9. Mean porosity in the core zone of the gauge section for (a) AP specimens and (b) MPP specimens in function of the orientation angle of the tensile test specimens, as measured by numerical data treatment of X-µCT images. Error bars represent the standard deviation of sectional porosity through the direction of deposition. Dash lines represent the minimum and maximum sectional porosity.

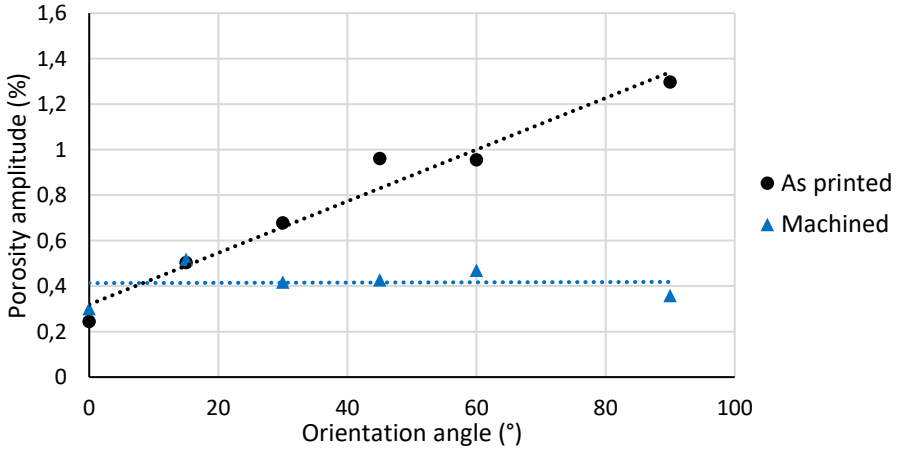

Figure 10. Difference between maximum and minimum sectional porosity in the core zone of the gauge section for AP specimens and MPP specimens in function of the orientation angle of the tensile test specimens, as measured by numerical data treatment of X-µCT images. Dot lines represent the linear regressions for comparison of the evolution of porosity amplitude in function of the orientation angle between AP and MPP specimens.

The microstructures of the AP specimens are dependent on orientation angle due to multiple physical phenomena, while the MPP specimens have more constant microstructures both in the whole part and regarding orientation angle. Inconstant microstructures for the AP specimens can lead to more than 40% difference in sectional porosity from one cut plane to another in the extremum case of 90° orientation angle, proving the necessity of X-µCT and/or the machining of a unique plate to study the intrinsic mechanical properties in a same structure without it being impacted by the porosity distribution or inter-raster adhesion. One should note that those microstructural observations can be extended to effective printed parts and be an indication of the deposition strategy influence on the microstructure.

3.2. Mechanical properties

The tensile tests at different raster angles are analyzed based on the comparison of stress-strain curves, Young's modulus, ultimate tensile strength, and fracture surfaces evolution as a function of raster angle for both AP and MPP specimens. The stress-strain curves displayed in Figure 11 highlight the printed PETG tensile behavior evolution according to raster angles. A classic behavior consisting of a linear stage followed by a nonlinear stage is observed.

(a)

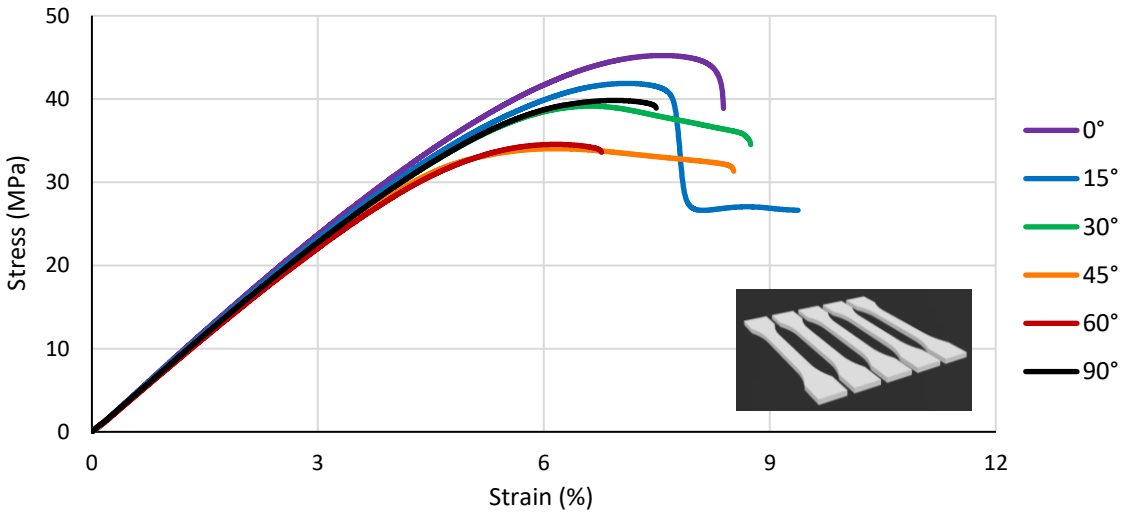

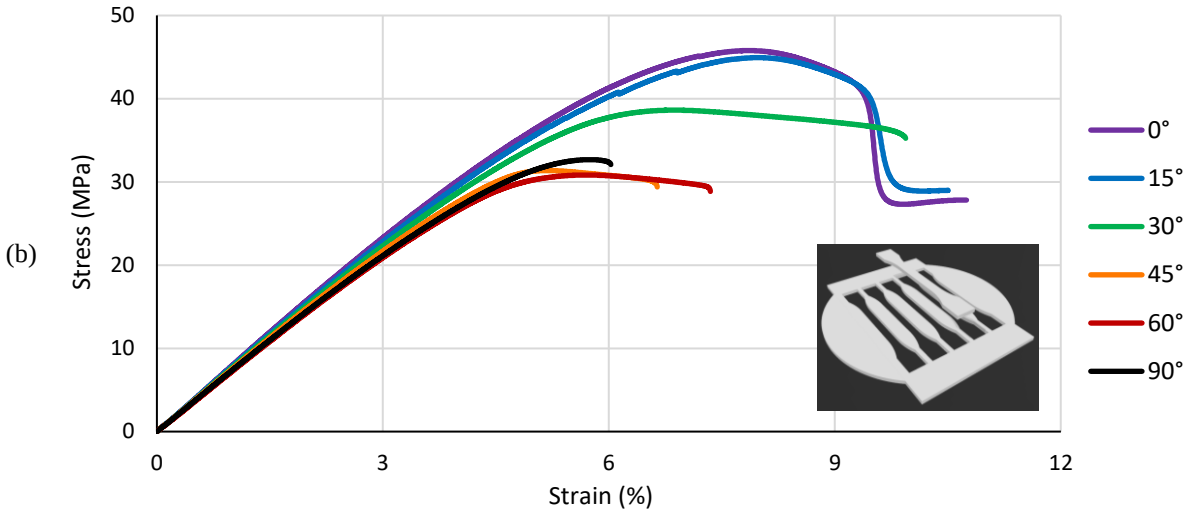

Figure 11. Representative tensile stress-strain curves at different orientation angles for printed PETG (a) AP specimens and (b) MPP specimens.

The Young's moduli are estimated through the linear stage and are presented in Figure 12(a). As already reported in the literature, increasing the orientation angle tends to decrease the Young's modulus of printed specimens [30], but the decrease is more pronounced for the MPP specimens, showing a sigmoid-like evolution, than for the AP ones (see Figure 12(a)) whose Young's modulus increases from 60° to 90°. The difference of rigidity between the AP and MPP specimens is statistically nil from 0 to 30° in orientation angle, but continuously increase from 45° to attain an 8.9% relative difference at 90°. The decrease in Young's modulus with orientation can be explained by the maximum porosity in the effective section, which increases with the raster angle. In addition, for the AP specimens compared to the MPP specimens, the evolution of the effective section with raster angle is also modified by fuller structures on the edges at the highest orientation angles that contribute to the overall rigidity of the parts (see Figure 7) [19,22] and lower porosity in the core zone (3.9% against 6%, see Figure 9). Then, the MPP specimens better characterize the anisotropic elastic behavior of the core zone material than the AP specimens. One must remark that the sigmoid-like evolution is also more consistent with theoretical models considering regular microstructures [31]. On the contrary, each of the AP specimen characterizes the tensile behavior of a specific part associated with specific printing conditions. The results are hardly extendable to other loadings.

The nonlinear stages (see Figure 11) of the tensile tests depend on the raster angle for both AP and MPP specimens. At 0° and 15°, the nonlinear phase shows a plastic behavior stage in the form of a plateau followed by a creep, which is typical of a ductile behavior with striction inherent to the linear polymers due to the polymer chain alignment into the loading direction [32]. On the contrary, at 90°, the stress-strain curves show less plasticity followed by a brittle fracture as the cavities act as crack initiation sites under mode I loadings, which can be worsen by weaker cohesive forces in the sintering zone between the rasters due to a low polymer chain entanglement compared to the core of the rasters [33]. This trend to a more brittle behavior, in addition to the decrease in rigidity when increasing the orientation angles, tends to decrease the toughness of the printed materials from 0° to 90°. 30°, 45° and 60° stress-strain curves show a transition from the 0° curve type to the 90° one with a decreasing plastic and creep stage before fracture. This transition is cleaner for the MPP specimens (see Figure 11(b)) than for the AP specimens (see Figure 11(a)) for which, e.g., the 90° specimens' brittle fracture occurs for lower strains than the 60° one. This observation can be explained by the differences in the

microstructures of the AP and MPP specimens detailed in Section 3.1. For the MPP specimens, all the specimens have the same microstructure and the same surface condition, thus the fracture behavior is only affected by the criticality of the loading on the crack initiation, which increases with raster angle. On the contrary, for the AP specimens, the evolution of the microstructure with raster angle and the surface condition influences the fracture behavior. For the 90° specimen, compared to the 60° one, the fracture initiation is delayed by the larger U-turn zone (see Figure 6), the lower porosity (see Figure 9(a)) and the more developed sintering. Thus, as for the Young's moduli, the MPP specimens actually characterize the core zone material fracture behavior while the AP specimens characterize the fracture behavior for particular printing conditions.

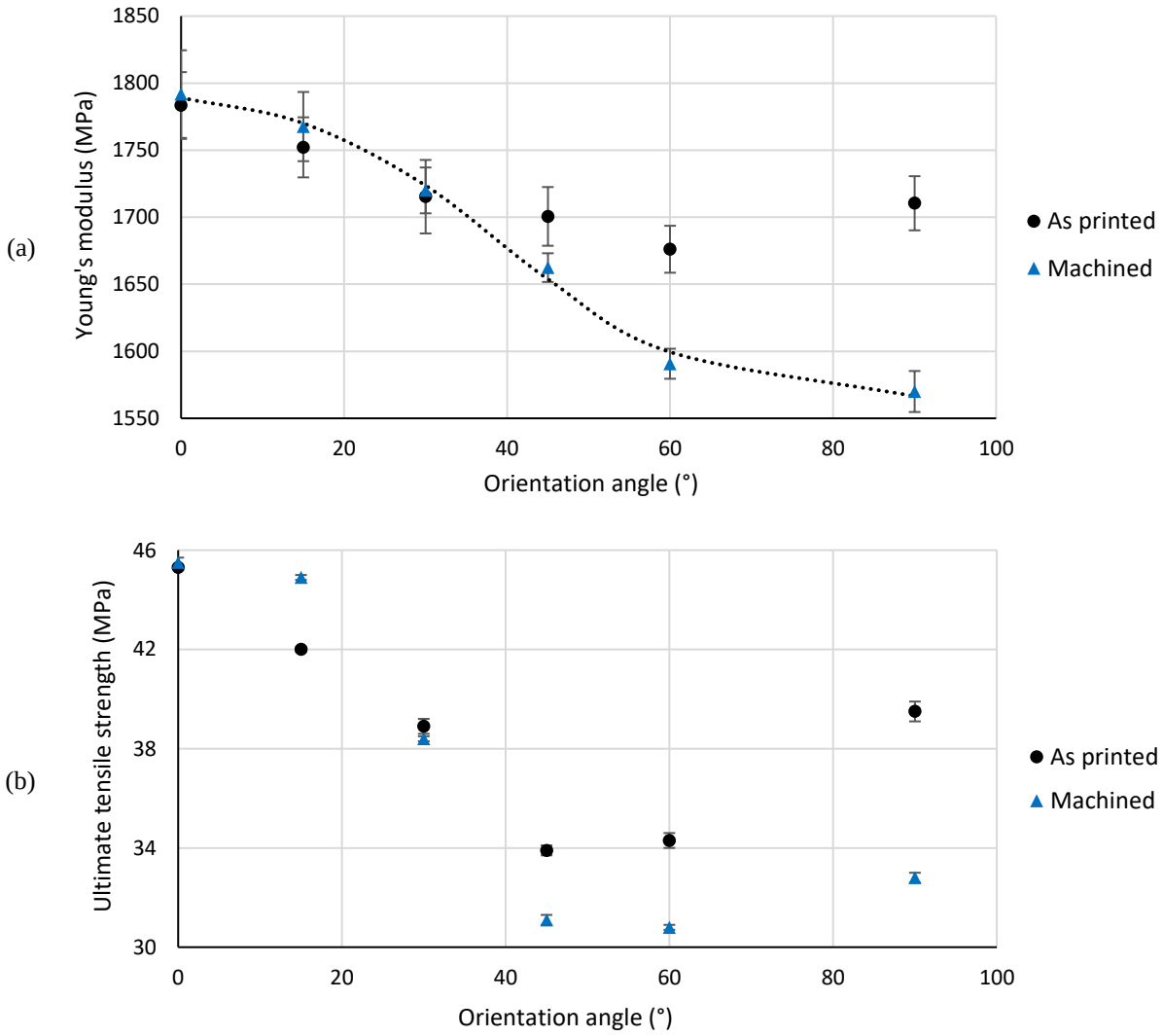

Figure 12. (a) Young's moduli and (b) ultimate tensile strengths plotted against the orientation angle of AP and MPP tensile test specimens. Error bars represent the standard deviations.

The ultimate tensile strengths of the specimens, presented in Figure 12(b), correspond to the plateau of the stress-strain curves. For all the specimens, this plateau is followed by a creep, which is eventually small but actually exists for every specimen, even for high raster angles, which suggests that the ultimate strength is not related to the crack initiation leading to the fracture of the specimen but to the interaction between the plastic behavior of the PETG and the cavities in the

specimens. At 0°, the alignment between the cavity direction and the tensile direction induces few stress concentrations in the microstructure (see 0° specimens in Figures 6 and 7). Then, the microscopic plastic strain is homogeneous in the microstructure and, thus, mainly in the core of the rasters where the PETG has the highest yield strength, while the weaker inter-raster zone is not loaded. Both stress concentration and load on the inter-raster zone are expected to increase with the raster angle and should induce a monotonic decrease in ultimate tensile strength with raster angle. This decrease is observed from 0° to 45°/60° for both AP and MPP specimens (see Figure 12(b)). The decrease from 0° to 15° is more pronounced for the AP specimens than for the MPP ones due to the increase in porosity from 0° to 15° for the AP specimens (see Figure 9(a)). The decrease is followed by an unexpected increase from 60° to 90°. A proper understanding of this phenomenon would require a complete study of the plastic strain and stress concentration in the microstructure. As a first approach, one can recall that, during a tensile test, the maximum shearing, which leads to plastic strain, is along the 45° plane. The maximum porosity in this plane is higher for both 45° and 60° specimens than for the 90° ones, which can explain why those specimens show a lower ultimate tensile strength than the 90° ones. The increase in ultimate tensile strength at 90° is more pronounced for the AP specimens, which can again be explained by edge reinforcement (see Figure 6), lower porosity (see Figure 9(a)) and more developed inter-raster sintering of the 90° AP specimens than for the 90° MPP specimens (see 90° specimens in Figures 6 and 7). This confirms that the preparation method for the AP specimens significantly impacts the measured mechanical properties and that a better characterization of the intrinsic mechanical properties of the core zone is obtained with the MPP preparation method. Moreover, in a modeling perspective, the fracture of the specimens is widely dependent on the defects and inhomogeneities in the microstructure. In that regard, the AP specimens are complex to model, while the homogeneity of the MPP specimens paves the way to a multiscale modeling based on a reduced representative volume element. Such model could help to understand the phenomenon involved in the fracture of the printed material and to determine, by an inverse method, the influent parameters such as the bonding strength between the rasters.

The observation of the fractured specimens displayed in Table 3 confirms the tendency observed in the stress-strain curves (see Figure 11), i.e. a progressive transition from a ductile fracture at 0° to a brittle one at 90°. The 0° and 15° specimens show striction phenomena and typical ductile fracture profiles due to the alignment of the linear polymer chains into the loading direction that leads to plastic strain and increased toughness. This profile is more clear and pronounced for the MPP specimens while the AP specimens show less striction before fracture and a plane fracture surface, which might come from the presence of stress concentrations at infill/perimeter intersections (see Figure 6) [34] and/or inhomogeneity of microstructural defects in the AP specimens (see Figures 6, 7 and 10) leading to fracture by crack initiation and/or propagation. The presence of more a pronounced striction for the MPP specimens is a clear indicator of the preponderance of the polymer material behavior, to the detriment of the edge microstructure effect, in the overall mechanical response of the specimens during tests. With the MPP specimens, the machining limits the crack initiation on edges by smoothing the surface (see MPP specimens in Figure 7) [35]. Again, the inhomogeneity of the AP specimens impacts its behavior and deteriorates the characteristics of the printed material. For the intermediate orientation angles, namely for the 30°, 45° and 60° AP and MPP specimens, a start of striction is observed before a brittle fracture with a fracture surface oriented along the raster orientation and multiple sub-fracture orientations for both AP and MPP specimens (see Table 3). The fracture seems to come from crack propagations along the inter-raster interface, as already observed in the literature for the highest orientation angles [36], that can be initiated at the angles of the hypotrochoid-like cavities (see Figure 7). Finally, at 90° for both AP and MPP specimens, a neat rupture takes place along inter-raster interface without any striction. This observation is explained by the low polymer chain entanglement at the raster-raster interface, compared to the entanglement

in the raster, which prevents polymer chain alignment caused and authorized by the sliding between polymer chains, and leads to the brittle behavior of the raster-raster interface at a 90° orientation angle, regardless of the preparation method. Globally, AP and MPP specimen fracture surfaces show the same evolution with raster angles from ductile fracture with striction at 0° to neat brittle fracture at 90°, but the MPP specimens undergo more striction due to a more regular microstructure and a better surface condition while the presence of defects in the AP specimens and their surface conditions facilitate the crack initiation leading to a brittle fracture.

Table 3. Comparison of the fracture location and profile of tested tensile test specimens at different orientations for AP and MPP specimens with associated photographic example of tested specimen. Red dashes represent the main direction of the fracture, in comparison to the blue lines representing the raster orientations.

	α (°)	Fracture location	Fracture profile	Photography
As-printed	0	Start of the reduced sections	Ductile with start of striction	
	15	Reduced and gauge sections	Ductile with start of striction	
	30	Gauge sections	Pseudo-brittle with multiple fracture orientations	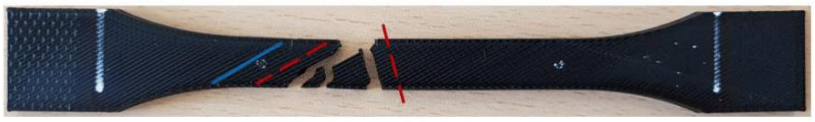
	45	Gauge sections	Pseudo-brittle with multiple fracture orientations	
	60	Reduced sections	Pseudo-brittle with multiple fracture orientations	
	90	Gauge sections	Brittle with neat fracture along inter-raster bond	
Machined	0	Limit of gauge sections	Ductile with striction	
	15	Limit of gauge sections	Ductile with striction	
	30	Gauge sections	Pseudo-brittle with multiple fracture orientations	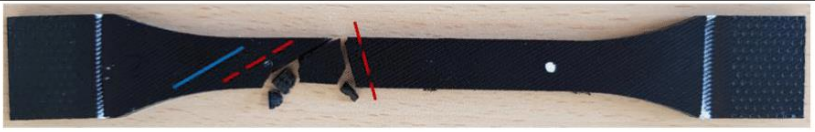
	45	Gauge sections	Pseudo-brittle with multiple fracture orientations	
	60	Gauge sections	Pseudo-brittle with multiple fracture orientations	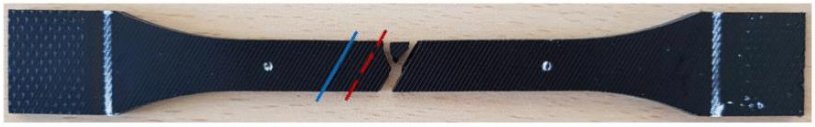
	90	Gauge sections	Brittle with neat fracture along inter-raster bond	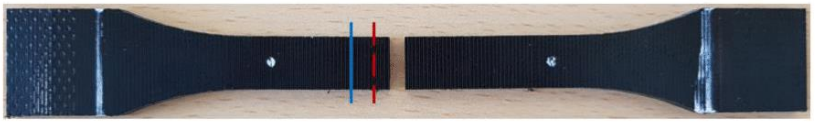

4. Conclusion and perspectives

A new method is proposed to prepare standardized specimens freed from the influence of both deposition strategy and printing conditions by machining tensile test specimens into printed plates from a unique design and standardized printing conditions. This hybrid method has been shown to be effective for having a low material health alteration and good surface finish conditions regarding machining process. A comparison with classical as-printed specimens highlights the significance of the standardization and the advantages of the new method.

A thorough investigation of the microstructures shows the regularity of the machined specimens compared to the as-printed specimens, whose microstructures are strongly impacted by the printing conditions and the deposition strategy. X-µCT analysis reveals the variability of the microstructure of the as-printed specimens in the core zone both in terms of porosity mean values and in terms of porosity oscillation due to flow instability and thermo-kinetic effects during the printing. An important edge modification of the microstructure is also observed due to U-turns and perimeter reinforcements. These microstructure variabilities have a significant influence on the tensile behavior of the specimens, which could cause bias in the characterization of process-properties relationships. While machined specimens characterize the actual intrinsic mechanical properties induced by a unique microstructure associated with controlled printing conditions, as-printed specimens allow the assessment of the edge and scale effects and the microstructure variability by comparison with machined specimens. Machined specimens are then more representative of parts with dimensions and designs involving a low edge-to-core ratio, while a high ratio would be better described regarding the mechanical response of as-printed specimens.

Thus, the proposed preparation method generates microstructurally and mechanically standardized tensile test specimens associated with given printing conditions, leading to reproductible and comparable characterizations of the printed material. It provides an appropriate basis to define a unified standard for the characterization of additively manufactured parts. Such hybrid preparation methods are expected to be developed with other materials and AM techniques concerning their singular specifications. Guidelines may be drawn from those standardized methods and help industrial part qualification in demanding applications such as aerospace or medical applications. Furthermore, in a modeling perspective, this preparation method paves the way to the separate characterization of the influence of the different printing parameters, then to an actual control of the process-properties relationships and the modeling of the coupling between the different phenomena, namely core zone behavior, edge effect, thermo-kinetic influence on the microstructure, etc., that lead to the actual behavior of printed parts.

5. Acknowledgements

This project is included in the MATUR Chair, co-financed by the Région Champagne-Ardenne (France) (grant number D201507798), the European Union (grant number D201507799) and UIMM (partners convention n°13-2015).

6. References

[1] S.A.M. Tofail, E.P. Koumoulos, A. Bandyopadhyay, S. Bose, L. O'Donoghue, C. Charitidis, Additive manufacturing: scientific and technological challenges, market uptake and opportunities, Mater. Today. 21 (2018) 22–37. https://doi.org/10.1016/j.mattod.2017.07.001.

[2] X. Gao, S. Qi, X. Kuang, Y. Su, J. Li, D. Wang, Fused filament fabrication of polymer materials: A review of interlayer bond, Addit. Manuf. 37 (2021) 101658. https://doi.org/10.1016/j.addma.2020.101658.

[3] J. Allum, A. Moetazedian, A. Gleadall, V.V. Silberschmidt, Interlayer bonding has bulk-material strength in extrusion additive manufacturing: New understanding of anisotropy, Addit. Manuf. 34 (2020) 101297. https://doi.org/10.1016/j.addma.2020.101297.

[4] T.D. Ngo, A. Kashani, G. Imbalzano, K.T.Q. Nguyen, D. Hui, Additive manufacturing (3D printing): A review of materials, methods, applications and challenges, Compos. Part B Eng. 143 (2018) 172–196. https://doi.org/10.1016/j.compositesb.2018.02.012.
[5] M. Srivastava, S. Rathee, V. Patel, A. Kumar, P.G. Koppad, A review of various materials for additive manufacturing: Recent trends and processing issues, J. Mater. Res. Technol. 21 (2022) 2612–2641. https://doi.org/10.1016/j.jmrt.2022.10.015.
[6] W. Gao, Y. Zhang, D. Ramanujan, K. Ramani, Y. Chen, C.B. Williams, C.C.L. Wang, Y.C. Shin, S. Zhang, P.D. Zavattieri, The status, challenges, and future of additive manufacturing in engineering, Comput.-Aided Des. 69 (2015) 65–89. https://doi.org/10.1016/j.cad.2015.04.001.
[7] G. Ginoux, I. Vroman, S. Alix, Influence of fused filament fabrication parameters on tensile properties of polylactide/layered silicate nanocomposite using response surface methodology, J. Appl. Polym. Sci. 138 (2021) 50174. https://doi.org/10.1002/app.50174.
[8] S. Bakrani Balani, F. Chabert, V. Nassiet, A. Cantarel, Influence of printing parameters on the stability of deposited beads in fused filament fabrication of poly(lactic) acid, Addit. Manuf. 25 (2019) 112–121. https://doi.org/10.1016/j.addma.2018.10.012.
[9] O.A. Mohamed, S.H. Masood, J.L. Bhowmik, Experimental Investigations of Process Parameters Influence on Rheological Behavior and Dynamic Mechanical Properties of FDM Manufactured Parts, Mater. Manuf. Process. 31 (2016) 1983–1994. https://doi.org/10.1080/10426914.2015.1127955.
[10] T.Q. Tran, F.L. Ng, J.T.Y. Kai, S. Feih, M.L.S. Nai, Tensile Strength Enhancement of Fused Filament Fabrication Printed Parts: A Review of Process Improvement Approaches and Respective Impact, Addit. Manuf. 54 (2022) 102724. https://doi.org/10.1016/j.addma.2022.102724.
[11] C. Casavola, A. Cazzato, V. Moramarco, C. Pappalettere, Orthotropic mechanical properties of fused deposition modelling parts described by classical laminate theory, Mater. Des. 90 (2016) 453–458. https://doi.org/10.1016/j.matdes.2015.11.009.
[12] A. Trofimov, J. Le Pavic, S. Pautard, D. Therriault, M. Lévesque, Experimentally validated modeling of the temperature distribution and the distortion during the Fused Filament Fabrication process, Addit. Manuf. 54 (2022) 102693. https://doi.org/10.1016/j.addma.2022.102693.
[13] Q. Sun, G.M. Rizvi, C.T. Bellehumeur, P. Gu, Effect of processing conditions on the bonding quality of FDM polymer filaments, Rapid Prototyp. J. 14 (2008) 72–80.
[14] G. Hsiang Loh, E. Pei, J. Gonzalez-Gutierrez, M. Monzón, An Overview of Material Extrusion Troubleshooting, Appl. Sci. 10 (2020) 4776. https://doi.org/10.3390/app10144776.
[15] A. Armillotta, M. Bellotti, M. Cavallaro, Warpage of FDM parts: Experimental tests and analytic model, Robot. Comput.-Integr. Manuf. 50 (2018) 140–152. https://doi.org/10.1016/j.rcim.2017.09.007.
[16] M. Spoerk, F. Arbeiter, H. Cajner, J. Sapkota, C. Holzer, Parametric optimization of intra- and inter-layer strengths in parts produced by extrusion-based additive manufacturing of poly(lactic acid), J. Appl. Polym. Sci. 134 (2017) 45401. https://doi.org/10.1002/app.45401.
[17] C. Bellehumeur, L. Li, Q. Sun, P. Gu, Modeling of Bond Formation Between Polymer Filaments in the Fused Deposition Modeling Process, J. Manuf. Process. 6 (2004) 170–178. https://doi.org/10.1016/S1526-6125(04)70071-7.
[18] R. Comminal, M.P. Serdeczny, D.B. Pedersen, J. Spangenberg, Motion planning and numerical simulation of material deposition at corners in extrusion additive manufacturing, Addit. Manuf. 29 (2019) 100753. https://doi.org/10.1016/j.addma.2019.06.005.
[19] Y. Zhang, J.P. Choi, S.K. Moon, Effect of geometry on the mechanical response of additively manufactured polymer, Polym. Test. 100 (2021) 107245. https://doi.org/10.1016/j.polymertesting.2021.107245.
[20] C. Phillips, M. Kortschot, F. Azhari, Towards standardizing the preparation of test specimens made with material extrusion: Review of current techniques for tensile testing, Addit. Manuf. 58 (2022) 103050. https://doi.org/10.1016/j.addma.2022.103050.
[21] L. Fang, Y. Yan, O. Agarwal, J.E. Seppala, K.D. Migler, T.D. Nguyen, S.H. Kang, Estimations of the effective Young's modulus of specimens prepared by fused filament fabrication, Addit. Manuf. 42 (2021) 101983. https://doi.org/10.1016/j.addma.2021.101983.
[22] C. Koch, L. Van Hulle, N. Rudolph, Investigation of mechanical anisotropy of the fused filament fabrication process via customized tool path generation, Addit. Manuf. 16 (2017) 138–145. https://doi.org/10.1016/j.addma.2017.06.003.
[23] Y. Song, Y. Li, W. Song, K. Yee, K.-Y. Lee, V.L. Tagarielli, Measurements of the mechanical response of unidirectional 3D-printed PLA, Mater. Des. 123 (2017) 154–164. https://doi.org/10.1016/j.matdes.2017.03.051.
[24] H. Nouri, S. Guessasma, S. Belhabib, Structural imperfections in additive manufacturing perceived from the X-ray micro-tomography perspective, J. Mater. Process. Technol. 234 (2016) 113–124. https://doi.org/10.1016/j.jmatprotec.2016.03.019.
[25] J.E. Seppala, S. Hoon Han, K.E. Hillgartner, C.S. Davis, K.B. Migler, Weld formation during material extrusion additive manufacturing, Soft Matter. 13 (2017) 6761–6769. https://doi.org/10.1039/C7SM00950J.

[26] Y. Tao, F. Kong, Z. Li, J. Zhang, X. Zhao, Q. Yin, D. Xing, P. Li, A review on voids of 3D printed parts by fused filament fabrication, J. Mater. Res. Technol. 15 (2021) 4860–4879. https://doi.org/10.1016/j.jmrt.2021.10.108.
[27] J. Kattinger, T. Ebinger, R. Kurz, C. Bonten, Numerical simulation of the complex flow during material extrusion in fused filament fabrication, Addit. Manuf. 49 (2022) 102476. https://doi.org/10.1016/j.addma.2021.102476.
[28] Y. Fu, X. Yao, A review on manufacturing defects and their detection of fiber reinforced resin matrix composites, Compos. Part C Open Access. 8 (2022) 100276. https://doi.org/10.1016/j.jcomc.2022.100276.
[29] R. van Weeren, M. Agarwala, V.R. Jamalabad, A. Bandyophadyay, N. Langrana, A. Safari, P. Whalen, C. Ballard, Quality of Parts Processed by Fused Deposition, (n.d.) 8.
[30] L. Li, Q. Sun, C. Bellehumeur, P. Gu, Composite Modeling and Analysis for Fabrication of FDM Prototypes with Locally Controlled Properties, J. Manuf. Process. 4 (2002) 129–141. https://doi.org/10.1016/S1526-6125(02)70139-4.
[31] R. Chen, A.F. Kaplan, D.G. Senesky, Closed-form orthotropic constitutive model for aligned square array mesostructure, Addit. Manuf. 36 (2020) 101463. https://doi.org/10.1016/j.addma.2020.101463.
[32] R.B. Dupaix, M.C. Boyce, Finite strain behavior of poly(ethylene terephthalate) (PET) and poly(ethylene terephthalate)-glycol (PETG), Polymer. 46 (2005) 4827–4838. https://doi.org/10.1016/j.polymer.2005.03.083.
[33] O.S. Carneiro, A.F. Silva, R. Gomes, Fused deposition modeling with polypropylene, Mater. Des. 83 (2015) 768–776. https://doi.org/10.1016/j.matdes.2015.06.053.
[34] T. Webbe Kerekes, H. Lim, W.Y. Joe, G.J. Yun, Characterization of process–deformation/damage property relationship of fused deposition modeling (FDM) 3D-printed specimens, Addit. Manuf. 25 (2019) 532–544. https://doi.org/10.1016/j.addma.2018.11.008.
[35] P. Striemann, D. Huelsbusch, M. Niedermeier, F. Walther, Application-oriented assessment of the interlayer tensile strength of additively manufactured polymers, Addit. Manuf. 46 (2021) 102095. https://doi.org/10.1016/j.addma.2021.102095.
[36] A. Garg, A. Bhattacharya, An insight to the failure of FDM parts under tensile loading: finite element analysis and experimental study, Int. J. Mech. Sci. 120 (2017) 225–236. https://doi.org/10.1016/j.ijmecsci.2016.11.032.